View Article Online
View Journal

Nanoscale Horizons

The home for rapid reports of exceptional significance in nanoscience and nanotechnology

Accepted Manuscript

This article can be cited before page numbers have been issued, to do this please use: B. Heitzer, J. Drenth, N. Bhalla, Z. Bradley and A. Ganguly, *Nanoscale Horiz.*, 2026, DOI: 10.1039/D6NH00145A.

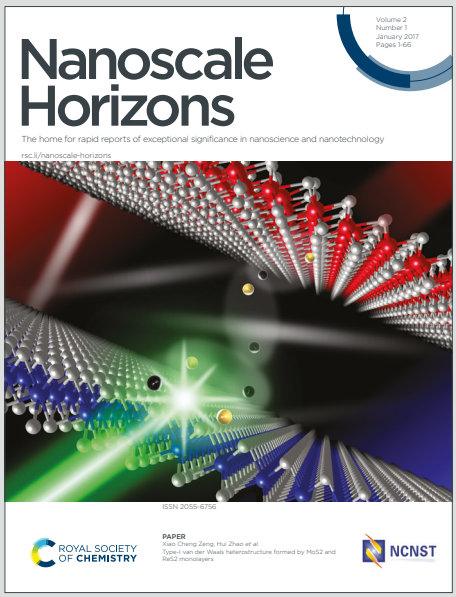

View Article Online
DOI: 10.1039/D6NH00145A

This manuscript introduces a groundbreaking framework for understanding how nanoparticle geometry influences interfacial thermal resistance in plasmonic nanostructures. By developing a geometry-driven scaling law, the work connects nanoparticle shape to thermal transport at the metal-liquid interface, establishing a predictive relationship that applies across various nanostructure morphologies—spheres, rods, and nanostars. The key innovation is the identification of a single dimensionless geometry factor that governs heat exchange, allowing for predictive design rules in thermoplasmonics, energy harvesting, and sensor systems. This work transcends material-specific or optical driving conditions, offering a robust, scalable approach for engineering heat flow in nanostructured systems.

View Article Online
DOI: 10.1039/D6NH00145A

Geometry Scaling of Thermal Boundary Resistance in Plasmonic Nanostructures

Zoe Bradley[1], Abhijit Ganguly[1], Bas Heitzer[2], Jaap Drenth[2], and Nikhil Bhalla*[1]

[1]Nanotechnology and Integrated Bioengineering Centre (NIBEC), School of Engineering, Ulster University, 2-24 York Street, Belfast BT15 1AP, Northern Ireland, United Kingdom

[2]Sensip-dx, Oxfordlaan 70, 6229 EV Maastricht, Netherlands

Abstract

Heat exchange between metal nanoparticles and their surrounding liquid plays a central role in thermoplasmonics, photonics, and nanoscale sensing. Yet it remains difficult to predict how particle shape influences interfacial thermal resistance. Here we introduce a geometry-driven scaling theory supported by experiments that identifies shape as the primary determinant of interfacial resistance and demonstrates that this resistance scales linearly with the number of nanoscale heat sources within a given fluid volume. Using a reduced single-time-constant description of thermal relaxation, time-domain measurements yield volume-normalised interfacial resistances independent of the surrounding fluid pathway. When expressed through appropriate geometric normalisation, these resistances fall onto a master scaling trend across nano stars, spheres,

*Corresponding author: n.bhalla@ulster.ac.uk

View Article Online
DOI: 10.1039/D6NH00145A

and rods. The resulting scaling law, $R_{\mathrm{int,vol}}(A_{\mathrm{NP}}/V_{\mathrm{NP}})/R_{K0}$ plotted against the geometry factor $D/L + \alpha\,(h_{\mathrm{spike}}/r_{\mathrm{tip}})$ unifies structures of these different shapes by linking their interfacial thermal behaviour to a single dimensionless geometry factor. This formulation shows that geometry sets the governing law for interfacial heat transport at the nanoscale, offering a compact design principle for engineering heat flow in a wide range of nanostructured systems.

Keywords: Thermoplasmonics; LSPR; Geometry-driven-scaling; Nanoparticles; Sensors

1 Introduction

Controlling heat flow across interfaces is central to the operation and reliability of modern nanoscale technologies from microelectronic cooling [1] and photothermal therapies [2] to catalytic conversion [3] and energy harvesting [4]. As device dimensions shrink, thermal transport increasingly depends not only on material composition but also on atomic structure [5], curvature [6], and confinement [7] of nano/ sub-nanoscale features. Interfaces, rather than bulk materials, often determine overall heat dissipation [8], yet our ability to predict and tune interfacial resistance remains limited [9]. Developing rules that connect nanoscale geometry to heat flow is therefore essential for both fundamental understanding and rational nanosale device design [10]. Plasmonic nanostructures offer a model platform for probing such effects. When illuminated, their localized surface plasmon resonances (LSPRs) concentrate electromagnetic energy into nanoscale volumes and efficiently transduce light into heat [11, 12]. This ability underpins applications in thermoplasmonics [13], nanophotonics [14], catalysis [15], and biosensing [16].

Nanoplasmonic materials are routinely tailored to optimise their optical and chemical performance as LSPRs are highly sensitive to morphology, nanoparticle size, shape, and surface chemistry, [17, 18]. Yet, despite extensive control over optical and chemical properties, the corresponding thermal behaviour, specifically how geometry dictates heat exchange at

View Article Online
DOI: 10.1039/D6NH00145A

metal–liquid boundaries, has lacked a compact and predictive description that unifies different nanoparticle architectures [19]. At the nanoscale, the total thermal resistance (R_{th}) for a colloidal dispersion reflects both a fluid pathway and a nanoparticle–liquid interface. In measurement, R_{th} is defined from the observed temperature difference across a controlled heat flux; conceptually, the interfacial portion is captured by a Kapitza resistance per unit area R_{K0} (material baseline), modified by geometry [20, 21]. Because geometry modulates surface curvature [22], path length [23], and hot-spot localisation [24], it should, in principle, dial the interfacial contribution. However, a simple, geometry-explicit law that is portable across spheres, rods, and stars has been missing.

Here we develop and test a generic framework that makes this connection explicit and experimentally tractable. Essentially in our test system we have nanoparticles of spherical/rod/star shapes suspended in the liquid (buffer in which they are prepared). We adopt a two-temperature description for electrons and lattice with strong electron–phonon coupling, and work in the limit where the relaxation is single-exponential with time constant τ. This yields a parameter-lean conversion from time series to absolute, volume-normalised resistances via $\tau = C_\ell R_{\mathrm{th,vol}}$, with C_ℓ the lattice volumetric heat capacity of the metal and $R_{\mathrm{th,vol}}$ represents the total thermal resistance normalised by the probed fluid volume and contains both the nanoparticle–liquid interfacial contribution and the device-level fluid contribution. We determine the device-specific fluid contribution once (from baseline measurements) and subtract it to isolate the interfacial term under both dark and illuminated conditions. We then derive and test a geometry-explicit law for the interfacial contribution to the volumetric R_{th} of plasmonic nanostructures in liquid:

$$R_{\mathrm{int,vol}} = N_p \, \frac{V_{\mathrm{NP}}}{A_{\mathrm{NP}}} \, R_{K0} \left(\frac{D}{L} + \alpha \, \frac{h_{\mathrm{spike}}}{r_{\mathrm{tip}}} \right) \tag{1}$$

where N_p is the nanoparticle number in the fluid, V_{NP}/A_{NP} encodes the base size dependence, R_{K0} is the material Kapitza resistance per unit area, and the bracketed term is a pure shape

View Article Online
DOI: 10.1039/D6NH00145A

factor set by spike height h_{spike} and tip radius r_{tip} (for rods and stars; it reduces to 1 for spheres). Please also note that V_{NP} is the volume of an individual nanoparticle, and A_{NP} is the surface area of an individual nanoparticle. Equation (1) predicts the following geometry collapse:

$$\frac{R_{\mathrm{int,vol}}\,(A_{\mathrm{NP}}/V_{\mathrm{NP}})}{R_{K0}} = N_p\left(\frac{D}{L} + \alpha\,\frac{h_{\mathrm{spike}}}{r_{\mathrm{tip}}}\right) \tag{2}$$

i.e., a straight line of slope N_p and zero intercept when the normalised interfacial term is plotted against the geometry factor. Here, R_{K0} denotes the baseline Kapitza resistance per unit area for the Au–buffer interface. It is treated as a material/interfacial reference parameter that is independent of nanoparticle geometry in the present model, see more details in the Supplementary Information. In the proceeding text, we present the extraction of τ and $R_{\mathrm{th,vol}}$, quantify and remove the device fluid term, and demonstrate the predicted collapse across spheres, rods, and nanostars. Full derivations and the identification protocol are provided in the Experimental Methods and Supplementary Information.

2 Results and Discussion

We first quantify the geometric descriptors that enter the scaling law and verify a stable operating window for all measurements. Scanning electron microscopy (SEM) establishes sizes for three archetypal Au nanostructures: spheres with diameter 35 ± 4 nm and area 3,892 nm^2, rods with length 55 ± 4 nm, diameter 10 ± 1 nm and area 14,951 nm^2 and stars with core 66 ± 10 nm, spike length 13.8 ± 2.3 nm and and area 10,589 nm^2, see Figure 1a)i (spheres), a)ii(rods), a)iii(stars) and b(area & volume). From these we compute the base $A_{\mathrm{NP}}/V_{\mathrm{NP}}$ and, for anisotropic stars, the inputs to the shape factor, namely spike height h_{spike} and tip radius r_{tip}, see Supplementary Information and Figure 1b. In experiments we employ a microfluidic heat-flow platform consisting of an aluminum (Al) sensor chip mounted on a 37°C copper (Cu) block with dual thermometry (substrate T_1, liquid T_2) and a constant heater power (heat-transfer rate) denoted by $\dot{Q}$ delivered by the electrical resistor,

View Article Online
DOI: 10.1039/D6NH00145A

Figure 1c,d. We define the measured thermal resistance as:

$$R_{\mathrm{th}} = \frac{T_1 - T_2}{\dot{Q}} \tag{3}$$

where $\dot{Q}$ has units of watts (W) and represents the net thermal power flowing from the heated block into the liquid through the device (i.e., heat rate rather than heat flux).

To rule out thermally induced restructuring as a confounder, we record absorbance from 30–40°C and observe modest amplitude changes (less than 0.1 absorbance units) with nearly fixed peak positions (no change in wavelength), as seen in Figure 1e. This confirms morphological stability over the test window and sets the geometric and thermal context for dynamical extraction of time constants next.

With geometry fixed, we next interrogate the thermal transport dynamics by analysing the time-dependent R_{th} trace, $R_m(t)$, defined as the instantaneous temperature difference divided by the applied power,

$$R_m(t) \equiv \frac{T_1(t) - T_2(t)}{P(t)} \tag{4}$$

where P is the total input power ($P = P_0$ in the dark and $P = P_0 + P_{\mathrm{abs}}$ under illumination, with P_0 the electrical heater power and P_{abs} the optically absorbed power). In the dark, the transient response is well described by a single exponential with a constant offset,

$$R_m(t) = R_0\, e^{-t/\tau} + C \tag{5}$$

where $R_0 \equiv R_m(0)$ is the initial value, $C \equiv R_m(\infty)$ is the nonzero steady baseline, and τ is the characteristic relaxation time obtained from fitting. Under illumination, the evolution follows

$$R_m(t) = R_\infty + \big(R_0 - R_\infty\big) e^{-t/\tau} \tag{6}$$

View Article Online
DOI: 10.1039/D6NH00145A

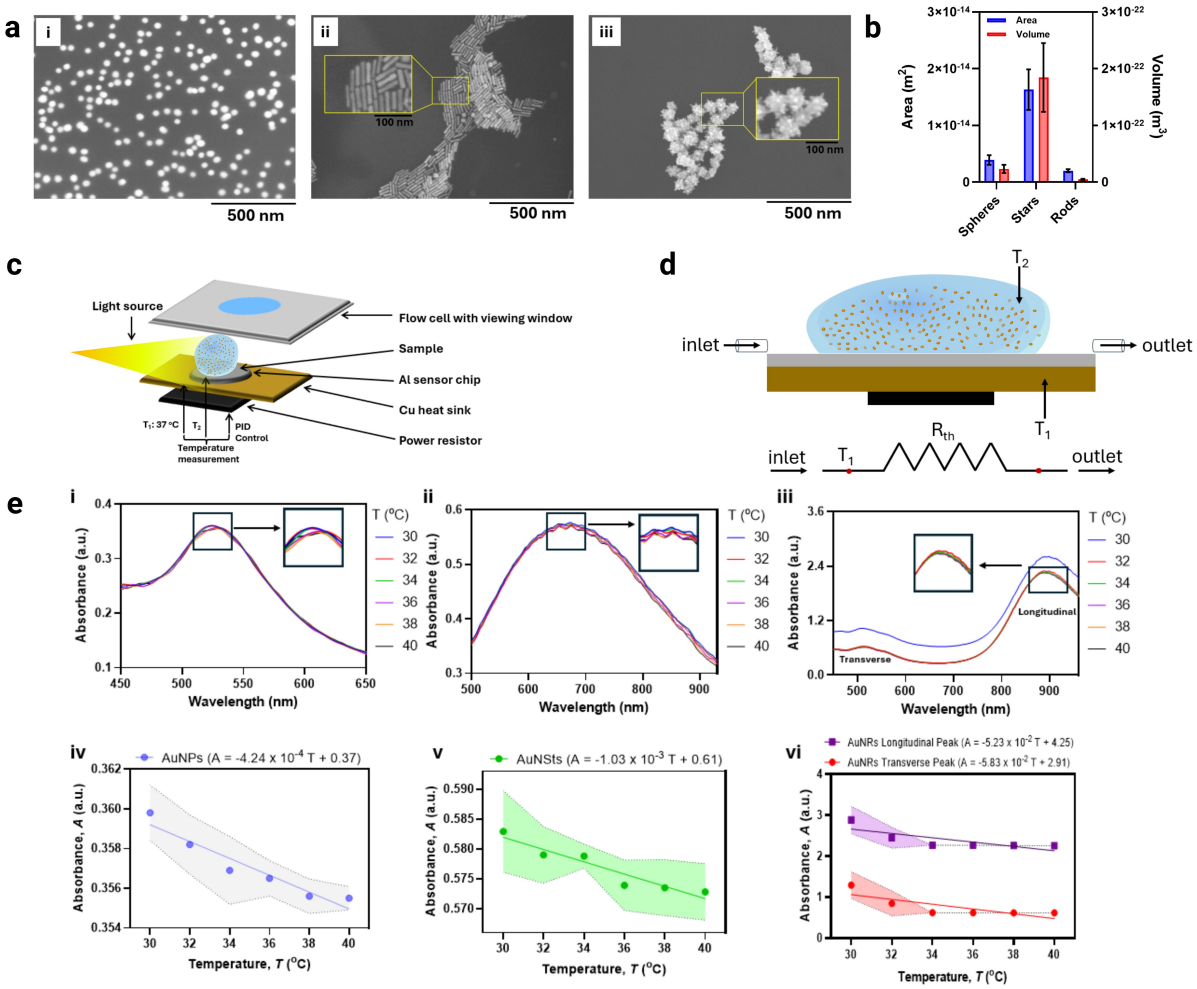

Figure 1: **Geometry and thermal–optical characterization of plasmonic nanostructures.** **(a)** Scanning electron micrographs of gold nanostructures: **(i)** nanospheres, **(ii)** nanorods, and **(iii)** nanostars. Scale bars: 500 nm. **(b)** Comparison of average particle surface area (left axis, blue) and volume (right axis, red) extracted from SEM image analysis. **(c)** Schematic of the temperature-controlled microfluidic platform used for thermal and optical measurements, comprising an aluminum sensor chip, copper heat sink, and PID-regulated heater. **(d)** Simplified cross-section showing fluid inlet/outlet and definition of measured temperatures T_1 and T_2 used to extract total R_{th}. **(e)** Temperature-dependent optical absorbance spectra of **(i)** nanospheres, **(ii)** nanostars, and **(iii)** nanorods recorded between 30 °C and 40 °C. Insets highlight the LSPR peak regions. Panels (iv–vi) summarise the corresponding peak absorbance $A(T)$ with linear fits (shaded ±95% confidence intervals), demonstrating minimal spectral drift and confirming morphological and optical stability across the experimental temperature range.

View Article Online
DOI: 10.1039/D6NH00145A

where R_∞ denotes the illuminated steady-state level, determined by power partitioning as

$$R_\infty = \frac{P_{\text{abs}}\, R_{\text{th}}}{P_0 + P_{\text{abs}}} \tag{7}$$

with R_{th} the total R_{th} (interface + fluid). The single time constant τ links directly to the overall resistance through the standard two-temperature reduction,

$$\tau = C_\ell R_{\text{th,vol}} \tag{8}$$

where C_ℓ is the volumetric lattice heat capacity of Au. Inclusion of the baseline term C in Eq. (5) avoids bias in τ and, consequently, in the derived R_{th} via Eq. (8). From the fitted τ values, we obtain both the absolute and volume-normalised R_{th}:

$$R_{\text{th,vol}} = \frac{\tau}{C_\ell}, \qquad R_{\text{th}} = \frac{R_{\text{th,vol}}}{V_{\text{fluid}}} \tag{9}$$

where V_{fluid} is the liquid volume of the measurement cell. Figure 2 summarises these dynamics 4 to 9. Figure 2a and b show experimental (dots) and fitted (lines) traces of $R_{\text{th}}(t)$ for nanospheres, nanostars, and nanorods under dark and illuminated conditions, respectively.

The single-exponential model captures the full time evolution with residuals close to the noise level, indicating that one dominant relaxation time is sufficient. Figures 2c(i)–(vi) compare experimental and modelled resistances on a point-by-point basis, confirming one-to-one correspondence across all morphologies and illumination states. Figure 2d compiles the corresponding R^2 values (> 0.90 in all cases), highlighting the robustness of the single-time-constant description. Illumination increases the apparent steady resistance, consistent with additional absorbed power and a shifted heat partition at the nanoparticle–liquid interface. The ordering is geometry-driven: nanostars exhibit the largest R_{th}, nanorods show the smallest dark–light contrast, and nanospheres lie in between. The excellent agreement between experiment and model allows us to fix the device fluid resistance term and isolate

View Article Online
DOI: 10.1039/D6NH00145A

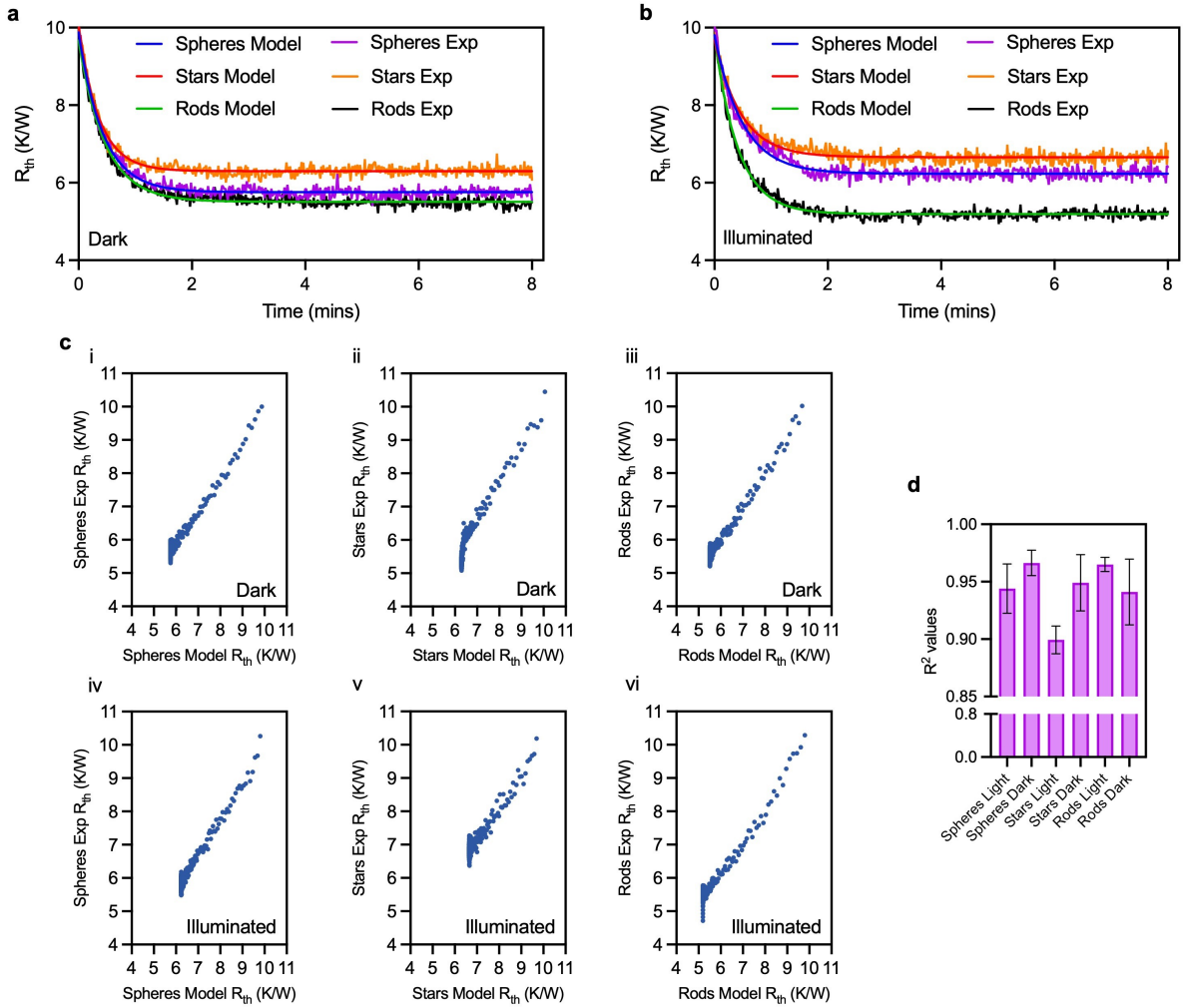

Figure 2: **Thermal relaxation dynamics and model validation.** **(a,b)** Experimental (dots) and modelled (lines) thermal resistance traces $R_{\mathrm{th}}(t)$ for Au nanospheres (blue), nanostars (green), and nanorods (magenta) under (a) dark and (b) illuminated conditions. **(c)** One-to-one comparison of experimental and modelled resistances for all morphologies: (i–iii) dark and (iv–vi) illuminated fits. **(d)** Coefficient of determination (R^2) values for each case, demonstrating high fidelity of the single-exponential model ($R^2 > 0.94$). Illumination increases the steady resistance through additional absorbed power, while a single relaxation time τ describes all data, validating the model and enabling isolation of the interfacial contribution in subsequent analysis.

View Article Online
DOI: 10.1039/D6NH00145A

the interfacial contribution $R_{\mathrm{int,vol}}$, enabling direct testing of the geometry-controlled scaling law developed below. In addition, the use of a single relaxation time is physically justified by the separation of timescales in the present system. Electron–phonon equilibration and intraparticle thermalisation in Au occur much faster than the experimentally resolved relaxation of the fluidic device. Therefore, over the measured time window, the electron and lattice temperatures can be treated as effectively equilibrated, reducing the two-temperature description to a single-temperature heat-transfer model governed by the dominant slower lattice/fluid relaxation pathway. The high R^2 values and absence of systematic deviation in the fitted traces further support the use of a single dominant relaxation time for extracting $R_{\mathrm{th,vol}}$.

To separate device effects from nanoscale interfacial transport, we first determine the fluid contribution using the dark response of deionised water ($\mathrm{dH_2O}$) (no nanoparticles). A single-τ fit yields the baseline fluid resistance R_{fluid} (Supplementary Information), which we convert to a volume-normalised quantity via

$$R_{\mathrm{fluid,vol}} = R_{\mathrm{fluid}}\, V_{\mathrm{fluid}} \tag{10}$$

For a measurement volume of $V_{\mathrm{fluid}} = 200\ \mu\mathrm{L}$ and $R_{\mathrm{fluid}} = 5.5\ \mathrm{K\,W^{-1}}$, this gives $R_{\mathrm{fluid,vol}} = 1.10 \times 10^{-6}\ \mathrm{m^3\,K\,W^{-1}}$. The same baseline may also be expressed in terms of an effective convection coefficient h_{conv} and wetted area A_{cell},

$$R_{\mathrm{fluid,vol}} = \frac{V_{\mathrm{fluid}}}{h_{\mathrm{conv}} A_{\mathrm{cell}}} \tag{11}$$

yielding $h_{\mathrm{conv}} \approx 2.3 \times 10^3\ \mathrm{W\,m^{-2}\,K^{-1}}$ for $A_{\mathrm{cell}} = \pi(5\ \mathrm{mm})^2$. Because neither the cell geometry nor the hydrodynamics change under illumination, this fluid baseline applies identically to all morphologies under both dark and light conditions. Having established the device

View Article Online
DOI: 10.1039/D6NH00145A

contribution, we isolate the nanoparticle–liquid interfacial term as

$$R_{\mathrm{int,vol}} = R_{\mathrm{th,vol}} - R_{\mathrm{fluid,vol}}, \tag{12}$$

with $R_{\mathrm{th,vol}} = \frac{\tau}{C_\ell}$ and $R_{\mathrm{th}} = \frac{\tau}{C_\ell V_{\mathrm{fluid}}}$ (as also discussed in the preceding text, Figure 2).

The fluid baseline was measured independently from the dH_2O control in the same cell geometry and thermal protocol and was treated as a fixed device/buffer contribution in the present analysis. This assumption affects the absolute magnitude of the extracted $R_{\mathrm{int,vol}}$, but because the same baseline is applied to all nanoparticle morphologies, it cannot by itself generate the observed morphology-dependent ordering. Future measurements should include repeated buffer-only runs to quantify the reproducibility of $R_{\mathrm{fluid,vol}}$ and propagate this uncertainty explicitly into $R_{\mathrm{int,vol}}$. It is important to note that $R_{\mathrm{fluid,vol}}$ is an independently measured device/buffer baseline obtained from the dH_2O control in the same measurement cell, rather than a morphology-dependent fitting parameter. Therefore, its subtraction removes a common additive contribution from all nanoparticle measurements. A fixed offset of this type cannot by itself generate the observed morphology-dependent ordering, because the relative differences between nanospheres, nanorods, and nanostars are already present in the measured total resistance before subtraction. The subtraction instead isolates the nanoparticle-associated contribution from the common macroscopic fluid pathway of the device.

Although local illumination may in principle modify near-particle viscosity, buoyancy, or microscale thermal transport, the measurement volume, cell geometry, temperature boundary condition, and illumination protocol were kept identical for all morphologies, and dark and illuminated datasets were analysed separately. Thus, any residual fluid contribution associated with a given measurement condition would act primarily as a common background rather than a shape-specific term. Under these conditions, the extracted $R_{\mathrm{int,vol}}$ represents the interfacial contribution after removal of the independently measured device/buffer re-

View Article Online
DOI: 10.1039/D6NH00145A

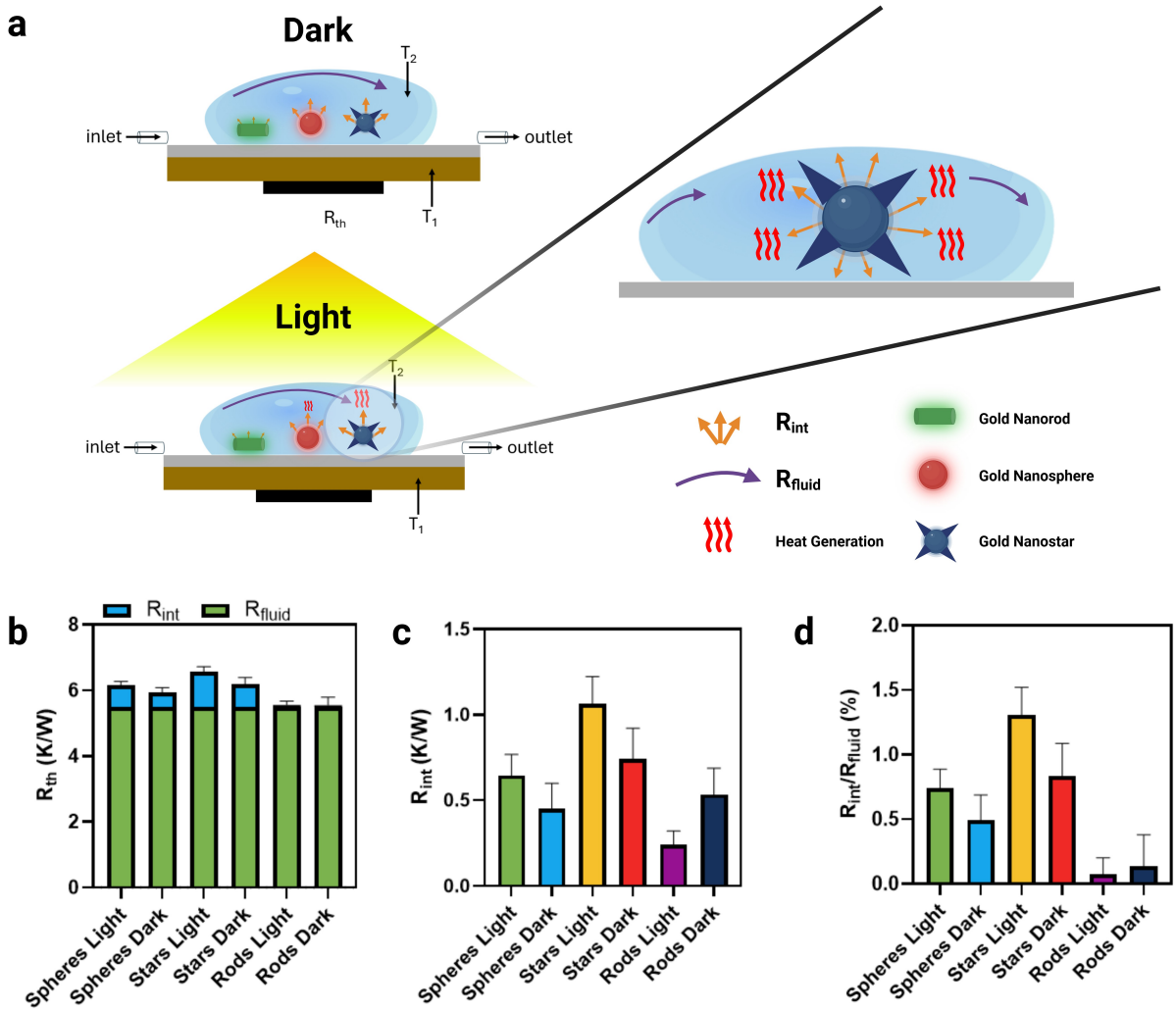

Figure 3: **Separation of fluid and interfacial thermal resistance components: (a)** Schematic illustrating the decomposition of the measured thermal resistance into a device-level fluid pathway and a geometry-dependent nanoparticle–liquid interfacial term under dark and illuminated conditions. **(b)** Measured total thermal resistances for nanospheres, nanostars, and nanorods, with the fixed fluid contribution R_{fluid} overlaid. **(c)** Extracted interfacial resistances R_{int} obtained by subtracting the fluid baseline from each measurement, revealing the morphology-driven ordering (nanostars > nanospheres > nanorods). **(d)** Ratio $R_{\text{int}}/R_{\text{fluid}}$, highlighting that geometry modulates the interfacial contribution whereas the fluid pathway remains constant across particle types and illumination states.

sistance. For systems involving different solvents, stronger optical heating, forced flow, or larger temperature gradients, $R_{\text{fluid,vol}}$ should be re-evaluated under the corresponding experimental conditions. Figure 3 brings together the consequences of this decomposition. Figure 3a illustrates the physical picture: the total R_{th} measured in our platform contains a

View Article Online
DOI: 10.1039/D6NH00145A

device-level fluid pathway and a morphology-dependent interfacial term. When we overlay the fixed fluid contribution onto the experimentally measured resistances (Figure 3b), the geometry dependence becomes immediately apparent. Subtracting this baseline yields the isolated interfacial resistances (Figure 3c), which follow a clear and intuitive ordering across morphologies: nanostars exhibit the largest interfacial resistance, nanospheres lie in the intermediate regime, and nanorods show the smallest values. The lower interfacial resistance observed for nanorods provides mechanistic insight into geometry-dependent heat transport and interfacial coupling in rod-like geometries. Gold nanorods have been shown experimentally and in simulations to exhibit efficient thermal coupling with surrounding liquids, where heat dissipation along their longitudinal axis enhances thermal transport relative to more isotropic shapes like spheres [25, 26]. Also, high-curvature features such as sharp tips and branches, typical of nanostars, can impede phonon coupling across the nanoparticle-liquid interface due to irregular structuring which ultimately enhances thermal resistance [27]. These geometric influences on interfacial heat transfer provide a physical basis for the geometry-dependent resistance hierarchy reported in Figure 3. This hierarchy persists under both dark and illuminated conditions, indicating that optical drive modifies the absolute resistance but not the relative role of geometry. Finally, examining the ratio $R_{\mathrm{int}}/R_{\mathrm{fluid}}$ (Figure 3d) highlights the same trend from a complementary perspective: while the fluid pathway remains constant, the interfacial contribution varies strongly with shape, confirming that geometry is the dominant control parameter for interfacial heat transport in these plasmonic systems.

This separation enables a direct test of the geometry-controlled law in the next section, where we plot the normalised interfacial term $R_{\mathrm{int,vol}}(A_{\mathrm{NP}}/V_{\mathrm{NP}}/R_{K0}$ against the single dimensionless shape factor $D/L + \alpha\, h_{\mathrm{spike}}/r_{\mathrm{tip}}$, with slope set by the nanoparticle number N_p. We test the central prediction by plotting the normalised interfacial term $y \equiv R_{\mathrm{int,vol}}(A/V)/R_{K0}$ against the dimensionless geometry factor $x \equiv D/L + \alpha\, h_{\mathrm{spike}}/r_{\mathrm{tip}}$ (Figure 4). The theory requires a single master line $y = N_p\, x$ whose slope is the nanoparticle number N_p and whose intercept is zero. To place uncertainties on both axes we propagate geometry and counting

View Article Online
DOI: 10.1039/D6NH00145A

errors by Monte Carlo using the measured size statistics (spheres: diameter, so $D = L$ and $x = 1$; rods: length L and diameter D, with no spikes so $h_{\mathrm{spike}} = 0$, $r_{\mathrm{tip}} = 0$ and $x = D/L$; stars: core diameter and spike parameters $h_{\mathrm{spike}}, r_{\mathrm{tip}}$) together with the independently determined uncertainty in N_p (see Experimental Methods section). We report asymmetric 95% confidence intervals (CIs) as horizontal (x) and vertical (y) error bars.

The horizontal CIs are notably larger for nanostars, which is expected: the shape factor contains a denominator through the spike term $\alpha\, h_{\mathrm{spike}}/r_{\mathrm{tip}}$, so small absolute uncertainty in r_{tip} (a few nanometres) translates into a large relative uncertainty in $h_{\mathrm{spike}}/r_{\mathrm{tip}}$. Together with the physical lower bound on r_{tip} (set by atomistic/ligand scales), this produces a right-skewed distribution for x, hence asymmetric CIs. Because the nanostar geometry factor contains $h_{\mathrm{spike}}/r_{\mathrm{tip}}$, it is particularly sensitive to uncertainty in the spike-tip radius. This uncertainty was included in the Monte Carlo propagation and leads to the broader, asymmetric confidence interval for nanostars. Thus, the nanostar point should be interpreted as an uncertainty envelope rather than a single deterministic geometry value. Within this propagated range, the nanostar data remain compatible with the same $y = N_p x$ scaling trend followed by spheres and rods. Spheres anchor the abscissa at $x \simeq 1$ (no spikes, $D = L$), rods occupy intermediate $x < 1$ values set by their aspect ratio D/L, and stars extend to much larger x dominated by the spike contribution. Vertically, the normalised ordinate y is insensitive to A/V and R_{K0} by construction; its spread is dominated by the uncertainty in N_p, which we visualise as a slope band for the line $y = N_p x$ (Figure 4). It should be noted that the normalised ordinate uses $R_{K0} = 5 \times 10^{-9}\,\mathrm{m^2K/W}$, which is chosen as a literature-consistent reference Kapitza resistance for the Au–buffer interface [28, 29, 30, 31]. This value is applied identically to nanospheres, nanorods, and nanostars and therefore acts only as a common normalisation factor. Further details on the choice of R_{K0} are provided in the Supplementary Information.

Despite the geometric uncertainties inherent to anisotropic structures, all three morphologies spheres, rods, and stars collapse onto a single common trend Figure 4. An orthogonal-

View Article Online
DOI: 10.1039/D6NH00145A

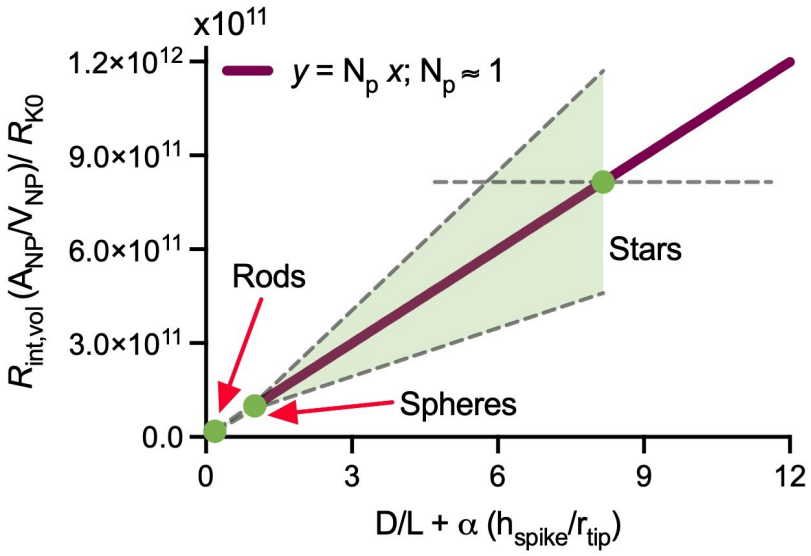

Figure 4: **Geometry scaling of interfacial thermal resistance.** Normalised interfacial resistance $R_{\mathrm{int,vol}}(A_{\mathrm{NP}}/V_{\mathrm{NP}}/R_{K0})$ plotted against the geometry factor $D/L+\alpha\,(h_{\mathrm{spike}}/r_{\mathrm{tip}})$ for nanospheres, nanorods, and nanostars. All morphologies collapse onto a single linear relation $y = N_p x$ (solid line), with slope set by the independently estimated total nanoparticle number within the probed fluid volume. Dashed guides indicate the allowed geometric envelope for each class of structure, and shaded regions reflect the uncertainty in spike height and tip radius for anisotropic particles. The collapse demonstrates that shape, not optical excitation or absolute size, governs the interfacial R_{th}, yielding a compact design rule for heat transport in plasmonic nanostructures.

distance regression, which accounts for errors in both axes, yields a slope statistically indistinguishable from the independently estimated total nanoparticle number N_p within the probed fluid volume, and an intercept consistent with zero, as predicted by the scaling law. Illumination modifies the absorbed optical power but leaves the collapse unchanged, demonstrating that geometry, not optical drive, governs the interfacial resistance. The spread in the nanostar data reflects the larger uncertainty in spike height and tip radius, yet the overall alignment with the master line confirms that the geometry factor captures the shape dependence of interfacial heat transport.

While the collapse supports a common geometry-controlled scaling trend across the three Au nanostructure classes studied here, we do not claim material-independent universality. The present validation is restricted to Au nanoparticles dispersed in aqueous media, with the

View Article Online
DOI: 10.1039/D6NH00145A

tested size range, ligand environment, particle concentration, illumination conditions, and device geometry. Changes in metal identity, surface chemistry, solvent composition, ionic strength, ligand shell thickness, aggregation state, or local convection may modify either the baseline Kapitza term or the fluid contribution. Therefore, the proposed relation should be viewed as a transferable scaling framework whose parameters must be re-established for each material–fluid–surface-chemistry system.

Conclusions

We have shown that interfacial heat transfer from plasmonic nanostructures follows a simple, predictive, and repeatable scaling law. When the volume-normalised interfacial term $y \equiv R_{\mathrm{int,vol}}(A_{\mathrm{NP}}/V_{\mathrm{NP}}/R_{K0})$ is expressed against the dimensionless geometry factor $x \equiv D/L + \alpha\,(h_{\mathrm{spike}}/r_{\mathrm{tip}})$, data from spheres, rods, and stars collapse onto the same linear trend, the same common slope, and the same geometry-controlled law. This collapse occurs repeatedly across diverse shapes and under both dark and illuminated conditions, reinforcing that geometry, and not the optical drive, determines the interfacial behaviour, with optical excitation altering absorbed power but not the underlying scaling. The physical interpretation is consistent: sharper curvature increases interfacial resistance, while normalisation by $A_{\mathrm{NP}}/V_{\mathrm{NP}}$ and R_{K0} removes material and size dependence, isolating pure shape. Even with explicit uncertainty propagation on both axes, the collapse persists; although extreme morphologies introduce broader spreads, all remain compatible with a shared slope set by independently measured N_p. Importantly, this scaling law enables geometry-first control of interfacial heat flow, where sharpening features or increasing N_p raises resistance, and blunting features or reducing N_p lowers it. The developed model, normalisation strategy and geometry factor are general and transferable, providing a compact and unifying framework for engineering nanoscale heat transport in thermoplasmonics, thermal metrology, and nanofluidic heat management. Future work could apply this framework to catalytic nanoparticles,

View Article Online
DOI: 10.1039/D6NH00145A

nanoscale heaters in biological media, or phase-change environments where interfacial heat flow governs performance. Extending the model to other materials, temperature regimes, or different geometries will further establish whether geometry-controlled thermal resistance can serve as a general design principle for heat management across nanoscale technologies.

3 Experimental Methods

3.1 Materials

Chemicals used include gold (III) chloride hydrate ($HAuCl_4$), sodium citrate tribasic (Na_3Cit), hydrochloric acid (HCl), nitric acid (HNO_3), potassium chloride (KCl), silver nitrate ($AgNO_3$), ascorbic acid ($C_6H_8O_6$, L-AA), sodium borohydride ($NaBH_4$), isopropanol, acetone, and phosphate buffered saline (PBS) were purchased from Merck Life Science, UK. Cetrimonium bromide ($CH_3(CH_2)_{15}N(Br)(CH_3)_3$, CTAB) was purchased from VWR, UK. 18.2 MΩ (dH_2O) from a Milli-Q Purification System (Sigma Aldrich, USA) was used throughout all experiments. All chemicals were used without further modification unless specified. All glassware was washed with aqua regia (HCl and HNO_3, in a 3:1 ratio), rinsed with dH_2O and dried before use.

3.2 Gold nanosphere synthesis

A modified version of the conventional Turkevich method was used to synthesize nanospheres [32]. Firstly, a 50 mL of 1 mM $HAuCl_4$ solution was heated to 90°C under continuous stirring. Once the solution reached 90°C, 2 mL of 38 mM Na_3Cit solution was added to the gold solution. A colour change from yellow to black to dark red was observed, indicating the formation of nanospheres. The nanoparticle solution was then allowed to cool to room temperature while stirring continuously. To wash the particles, 500 μL aliquots of the solution were centrifuged at 3600 g for 10 minutes, after which the supernatant was removed and the nanoparticle pellet was resuspended in dH_2O. This washing step was repeated a second

View Article Online
DOI: 10.1039/D6NH00145A

time to ensure purity. The purified nanospheres were stored away from light at 4°C before further use.

3.3 Gold nanostar synthesis

Nanostar synthesis was completed using the following protocol [33]. First, 25 μL of 100 mM $HAuCl_4$ and 5 μL of 2 M HCl were added to 10 mL of dH_2O under continuous stirring. Simultaneously, 75 μL of nanospheres, 100 μL of 3 mM $AgNO_3$, and 50 μL of 100 mM L-AA were added to the solution while stirring. A colour change from colourless to blue was observed, indicating the formation of nanostars. To stabilise the formed nanoparticles, 100 μL of 1 mM Na_3Cit was added. The solution was then centrifuged in 500 μL aliquots at 4180 g for 35 minutes, after which the supernatant was removed and the nanoparticle pellet was resuspended in dH_2O. This washing step was repeated a second time to ensure purity. The purified nanostars were stored away from light at 4°C before further use.

3.4 Gold nanorod synthesis

For single crystal nanorods synthesis, the following protocol was used under a constant temperature of 30°C [34]. CTAB seeds were synthesised by adding 25 μL of 50 mM $HAuCl_4$ solution to 4.7 mL of 0.1 M CTAB solution. The solution was stirred for 5 minutes before rapidly injecting 300 μL of 10 mM $NaBH_4$ under vigorous stirring at 400 rpm. After 20 seconds, the stirring of the CTAB seed solution was reduced to 80 rpm and maintained at this speed before use. To prepare the nanorods growth solution, 190 μL of 1 M HCl and 100 μL of 50 mM $HAuCl_4$ solution were added to 10 mL of 0.1 M CTAB, and the mixture was stirred at 400 rpm for 5 minutes. Under gentle stirring at 80 rpm, 120 μL of 10 mM $AgNO_3$ solution was added to the growth solution, followed by 100 μL of 100 mM L-AA. Next, 24 μL of the prepared CTAB seeds were added to the nanorod growth solution and stirred at 400 rpm for 20 seconds. The nanorod growth solution was then left undisturbed at 30°C for 3 hours to allow the nanorods to grow. The solution was centrifuged in 500 μL

View Article Online
DOI: 10.1039/D6NH00145A

aliquots at 8000 rpm for 10 minutes at 30°C, after which the supernatant was removed and the nanoparticle pellet was resuspended in dH_2O. This washing step was repeated a second time to ensure purity. The final single crystal nanorod product was stored at 30°C away from light.

3.5 Scanning electron microscope

Gold nanoparticle samples were characterised using a SU5000 SEM, from Hitachi, Japan paired with EM Wizard software for image acquisition. All images were acquired at an accelerating voltage of 10 kV, with a working distance of 3 mm and a spot intensity of 10. Prior to SEM imaging, liquid nanoparticle samples were prepared by drop-casting onto silicon wafers and were allowed to dry before analysis. From SEM images, ImageJ software was used to measure the size of each nanoparticle to measure the size and visually assess the particle geometry and dispersity.

3.6 Absorbance measurements

To understand the effect of temperature on nanoparticle absorbance, 200 μL aliquots of each sample were transferred to a clear 12-well microplate and their absorbance at 562 nm was measured over a temperature range of 30–40°C using a Tecan Spark spectrophotometer (Tecan Group Ltd., Männedorf, Switzerland).

3.7 Thermal resistance measurements

R_{th} measurements were conducted using a heat-transfer device from Sensip Dx, The Netherlands. An Al sensor chip was carefully positioned on a Cu block, which functioned as a stable heat source due to its high thermal mass and excellent thermal conductivity. Heat flow was generated via a 22 kΩ power resistor, which was mechanically fixed to the underside of the Cu block using heat-conductive silver (Ag) paste to ensure optimal thermal contact. During

View Article Online
DOI: 10.1039/D6NH00145A

the entire measurement process, the Cu block temperature was maintained at 37°C using an integrated temperature controller. Temperature measurements were obtained using two miniature thermocouples, each with a resistance of 10 kΩ for enhanced sensitivity and minimal response time. Thermocouple T_1 was embedded inside the Cu block directly beneath the Al sensor to monitor the heat source temperature, while T_2 was positioned within the liquid sample contained in the flow cell to measure the temperature of the sample medium. Experiments were performed under both illuminated and dark conditions. For each run, the sample was injected into the flow cell and allowed to equilibrate for 10 minutes to ensure thermal stability and eliminate transient effects. As a control, dH_2O was used as a reference in all experiments, allowing for normalisation and accurate comparison of R_{th} changes induced by the samples.

Monte Carlo uncertainty analysis in scaling procedure

To quantify how geometric and measurement uncertainties propagate into the dimensionless scaling relation, we performed a Monte Carlo analysis using Matlab R2025b, in which all experimentally determined parameters were randomly sampled according to their measured means and standard deviations. A total of 5×10^4 realisations were generated for each particle morphology (spheres, rods, and stars). For each parameter p, a truncated normal variate $p = \max(\varepsilon,\, p_\mu + p_\sigma \xi)$ with $\xi \sim \mathcal{N}(0,1)$ was used to prevent non-physical negative dimensions. The sampled quantities included the total number of particles N_p in the probed volume and all relevant geometric descriptors (particle diameters and lengths, spike heights, and tip radii), while fixed constants such as R_{K0} and α were treated as deterministic unless otherwise specified. For every realisation, we computed the morphology factor $g = \frac{D}{L} + \alpha\left(\frac{h_{\mathrm{spike}}}{r_{\mathrm{tip}}}\right)$, which equals unity for spheres and captures nanoscale interfacial enhancement for rods and stars. Using the experimentally established scaling law $R_{\mathrm{int,vol}}(A_{\mathrm{NP}}/V_{\mathrm{NP}}/R_{K0} = N_p g$, the dimensionless ordinate was evaluated as $y = N_p g$, while the morphology factor served as the abscissa $x = g$. From the resulting distributions, we extracted mean values, symmetric

View Article Online
DOI: 10.1039/D6NH00145A

standard deviations for x, and asymmetric 95% confidence intervals for y. To visualise the uncertainty in the predicted master curve, we computed the 95% confidence interval of N_p and plotted the corresponding slope band $y = N_p x$. The collapsed data points for spheres, rods, and stars, together with their propagated uncertainties, were then compared against this theoretical band, demonstrating that all morphologies follow the same linear scaling behavior.

Acknowledgments

The authors gratefully acknowledge the support provided through the Natural Environment Research Council (NERC) Award number: UKRI3237.

References

[1] Qun Jin, Tianxiao Guo, Nicolás Pérez, Nianjun Yang, Xin Jiang, Kornelius Nielsch, and Heiko Reith. On-chip micro temperature controllers based on freestanding thermoelectric nano films for low-power electronics. *Nano-Micro Letters*, 16(1):126, 2024.

[2] Ashutosh Giri, Scott G Walton, John Tomko, Niraj Bhatt, Michael J Johnson, David R Boris, Guanyu Lu, Joshua D Caldwell, Oleg V Prezhdo, and Patrick E Hopkins. Ultrafast and nanoscale energy transduction mechanisms and coupled thermal transport across interfaces. *ACS nano*, 17(15):14253–14282, 2023.

[3] Fernando Fresno, Ana Iglesias-Juez, and Juan M Coronado. Photothermal catalytic co_2 conversion: beyond catalysis and photocatalysis. *Topics in Current Chemistry*, 381(4):21, 2023.

[4] Baoping Zhang, Wanghuai Xu, Liang Peng, Yuchao Li, Wei Zhang, and Zuankai Wang. Nature-inspired interfacial engineering for energy harvesting. *Nature Reviews Electrical Engineering*, 1(4):218–233, 2024.

View Article Online
DOI: 10.1039/D6NH00145A

[5] Xiangrui Li, Wentao Chen, and Gyoko Nagayama. Interfacial thermal resonance in an sic–sic nanogap with various atomic surface terminations. *Nanoscale*, 15(19):8603–8610, 2023.

[6] Zhongwei Zhang, Jie Chen, and Baowen Li. Negative gaussian curvature induces significant suppression of thermal conduction in carbon crystals. *Nanoscale*, 9(37):14208–14214, 2017.

[7] Azmil Haris Azhar, Yusei Kobayashi, Takahiro Ikeda, and Masashi Yamakawa. Self-assembly and thermal conductivity of amphiphilic janus nanoparticles under nanoslit confinement. *RSC Advances*, 15(29):23588–23595, 2025.

[8] Ying Cui, Zihao Qin, Huan Wu, Man Li, and Yongjie Hu. Flexible thermal interface based on self-assembled boron arsenide for high-performance thermal management. *Nature Communications*, 12(1):1284, 2021.

[9] Ping Zhang, Peng Yuan, Xiong Jiang, Siping Zhai, Jianhua Zeng, Yaoqi Xian, Hongbo Qin, and Daoguo Yang. A theoretical review on interfacial thermal transport at the nanoscale. *Small*, 14(2):1702769, 2018.

[10] Xin Wu and Masahiro Nomura. Mathematically inspired structure design in nanoscale thermal transport. *Nanoscale*, 2025.

[11] Julian Gargiulo, Matias Herran, Ianina L. Violi, Ana Sousa-Castillo, Luciana P. Martinez, Simone Ezendam, Mariano Barella, Helene Giesler, Roland Grzeschik, Sebastian Schlücker, Stefan A. Maier, Fernando D. Stefani, and Emiliano Cortés. Impact of bimetallic interface design on heat generation in plasmonic au/pd nanostructures studied by single-particle thermometry. *Nature Communications*, 14(1):3813, 2023.

[12] Guillaume Baffou, Julien Polleux, Hervé Rigneault, and Serge Monneret. Super-heating and micro-bubble generation around plasmonic nanoparticles under cw illumination. *The Journal of Physical Chemistry C*, 118(9):4890–4898, 2014.

View Article Online
DOI: 10.1039/D6NH00145A

[13] Lixia Sang, Chong Wang, Yue Zhao, and Zhiyong Ren. Thermoplasmonics effect of au and ag multi-nanoparticles: Influence of polarized light direction, particle spacing, and substrates. *The Journal of Physical Chemistry C*, 127(30):14666–14678, 2023.

[14] Juan Wang, Stefan A Maier, and Andreas Tittl. Trends in nanophotonics-enabled optofluidic biosensors. *Advanced Optical Materials*, 10(7):2102366, 2022.

[15] Gayatri Joshi, Ab Qayoom Mir, Arkaprava Layek, Afsar Ali, Sk Tarik Aziz, Saumyakanti Khatua, and Arnab Dutta. Plasmon-based small-molecule activation: a new dawn in the field of solar-driven chemical transformation. *ACS Catalysis*, 12(2):1052–1067, 2022.

[16] Weizheng Wang, Youngsang You, and Sundaram Gunasekaran. Lspr-based colorimetric biosensing for food quality and safety. *Comprehensive Reviews in Food Science and Food Safety*, 20(6):5829–5855, 2021.

[17] Yingjie Hang, Anyang Wang, and Nianqiang Wu. Plasmonic silver and gold nanoparticles: shape-and structure-modulated plasmonic functionality for point-of-caring sensing, bio-imaging and medical therapy. *Chemical Society Reviews*, 53(6):2932–2971, 2024.

[18] Jiapeng Zheng, Xizhe Cheng, Han Zhang, Xiaopeng Bai, Ruoqi Ai, Lei Shao, and Jianfang Wang. Gold nanorods: the most versatile plasmonic nanoparticles. *Chemical Reviews*, 121(21):13342–13453, 2021.

[19] Guillaume Baffou and Romain Quidant. Thermo-plasmonics: using metallic nanostructures as nano-sources of heat. *Nature Materials*, 19:946–958, 2020.

[20] Mingxuan Jiang, Aidan Chapman, Juan D Olarte-Plata, and Fernando Bresme. Controlling local thermal gradients at molecular scales with janus nanoheaters. *Nanoscale*, 15(24):10264–10276, 2023.

[21] Jie Chen, Xiangfan Xu, Jun Zhou, and Baowen Li. Interfacial thermal resistance: Past, present, and future. *Reviews of Modern Physics*, 94(2):025002, 2022.

View Article Online
DOI: 10.1039/D6NH00145A

[22] Zhongqian Xi, Rui Zhang, Fabian Kiessling, Twan Lammers, and Roger M Pallares. Role of surface curvature in gold nanostar properties and applications. *ACS Biomaterials Science & Engineering*, 10(1):38–50, 2023.

[23] Priscilla Choo, Tingting Liu, and Teri W Odom. Nanoparticle shape determines dynamics of targeting nanoconstructs on cell membranes. *Journal of the American Chemical Society*, 143(12):4550–4555, 2021.

[24] Xiaofeng Zhou, Siqiao Liu, Hailang Xiang, Xiwang Li, Chunyan Wang, Yu Wu, and Gen Li. Three-dimensional sers substrates: Architectures, hot spot engineering, and biosensing applications. *Biosensors*, 15(9):555, 2025.

[25] Jonglo Park, Jingyu Huang, Wei Wang, Catherine J Murphy, and David G Cahill. Heat transport between au nanorods, surrounding liquids, and solid supports. *The Journal of Physical Chemistry C*, 116(50):26335–26341, 2012.

[26] Xuewang Wu, Yuxiang Ni, Jie Zhu, Nathan D Burrows, Catherine J Murphy, Traian Dumitrica, and Xiaojia Wang. Thermal transport across surfactant layers on gold nanorods in aqueous solution. *ACS applied materials & interfaces*, 8(16):10581–10589, 2016.

[27] Blake A Wilson, Steven O Nielsen, Jaona H Randrianalisoa, and Zhenpeng Qin. Curvature and temperature-dependent thermal interface conductance between nanoscale gold and water. *The Journal of Chemical Physics*, 157(5), 2022.

[28] Xi Chen, Ante Munjiza, Kai Zhang, and Dongsheng Wen. Molecular dynamics simulation of heat transfer from a gold nanoparticle to a water pool. *The Journal of Physical Chemistry C*, 118(2):1285–1293, 2014.

[29] Samy Merabia, Sergei Shenogin, Laurent Joly, Pawel Keblinski, and Jean-Louis Barrat. Heat transfer from nanoparticles: A corresponding state analysis. *Proceedings of the National Academy of Sciences*, 106(36):15113–15118, 2009.

View Article Online
DOI: 10.1039/D6NH00145A

[30] Oscar Gutiérrez-Varela, Bladimir Ramos-Alvarado, and Satish Kumar. Size-dependent effects of the thermal transport at gold nanoparticle–water interfaces. *The Journal of Chemical Physics*, 157(8):084702, 2022.

[31] Reza Rabani, Mohammad Hassan Saidi, Ali Rajabpour, Laurent Joly, and Samy Merabia. Enhanced heat flow between charged nanoparticles and an aqueous electrolyte. *Langmuir*, 39(43):15222–15230, 2023.

[32] J. Kimling, M. Maier, B. Okenve, V. Kotaidis, H. Ballot, and A. Plech. Turkevich method for gold nanoparticle synthesis revisited. *The Journal of Physical Chemistry B*, 110(32):15700–15707, 2006.

[33] Javier Lou-Franco, Yunfeng Zhao, Joost LD Nelis, Linda Stewart, Karen Rafferty, Christopher Elliott, and Cuong Cao. Smartphone-based immunochemical sensor exploiting peroxidase-like activity of ligand-capped gold nanostars: a proof-of-concept detection of mycobacterium bovis. *Biosensors and Bioelectronics*, 220:114857, 2023.

[34] Leonardo Scarabelli, Ana Sánchez-Iglesias, Jorge Pérez-Juste, and Luis M. Liz-Marzán. A "tips and tricks" practical guide to the synthesis of gold nanorods. *The Journal of Physical Chemistry Letters*, 6(21):4270–4279, 2015.

View Article Online
DOI: 10.1039/D6NH00145A

All experimental data is shared in this work and any other related data is available on request to corresponding authors.

Nikhil Bhalla